

The International Journal of Robotics Research

<http://ijr.sagepub.com>

Modeling and Control of Untethered Biomicrobots in a Fluidic Environment Using Electromagnetic Fields

K. Berk Yesin, Karl Vollmers and Bradley J. Nelson
The International Journal of Robotics Research 2006; 25; 527
DOI: 10.1177/0278364906065389

The online version of this article can be found at:
<http://ijr.sagepub.com/cgi/content/abstract/25/5-6/527>

Published by:

 SAGE Publications

<http://www.sagepublications.com>

On behalf of:



Multimedia Archives

Additional services and information for *The International Journal of Robotics Research* can be found at:

Email Alerts: <http://ijr.sagepub.com/cgi/alerts>

Subscriptions: <http://ijr.sagepub.com/subscriptions>

Reprints: <http://www.sagepub.com/journalsReprints.nav>

Permissions: <http://www.sagepub.com/journalsPermissions.nav>

K. Berk Yesin
Karl Vollmers
Bradley J. Nelson

Institute of Robotics and Intelligent Systems
ETH Zürich, 8092 Zürich, Switzerland
byesin@ethz.ch
kvollmers@ethz.ch
bnelson@ethz.ch
www.iris.ethz.ch

Modeling and Control of Untethered Biomicrorobots in a Fluidic Environment Using Electromagnetic Fields

Abstract

This paper investigates fundamental design, modeling, and control issues related to untethered biomedical microrobots guided inside the human body through external magnetic fields. Proposed areas of application for these microrobots include sensing, diagnosis, and surgical procedures in intraocular, cardiovascular, and inner-ear environments. A prototype microrobot and steering system are introduced. Fluid drag experiments performed on the prototype robot show that the $950 \times 400 \mu\text{m}$ elliptical shape has a spherical equivalent diameter of $477 \mu\text{m}$. Drag forces combined with saturation magnetization ($5 \times 10^5 \text{ A/m}$) of the prototype indicate that the required magnetic field gradients for application inside the vitreous humor and blood vessels are on the order of 0.7 T/m .

KEY WORDS—biomedical, microrobotics, wireless microrobot, magnetic microrobot, MEMS, microassembly

1. Introduction

The state-of-the-art in MEMS technology is progressing from individual, chip-level microsensors and microactuators to integrated systems. These types of systems will impact future minimally invasive surgical techniques by providing sub-mm untethered biomedical microrobots capable of performing a number of new procedures. The benefit will be even less injury to the patient resulting in faster recovery times. Proven MEMS technologies such as micro-needles, micro-pumps, and force and chemical sensors will be carried on-board for a variety of surgical and diagnostic tasks. Possible areas of application for these microrobots include intraocular, cardio-

vascular, and inner-ear sensing, diagnosis, and surgery. The treatment of retinal vein occlusions is one procedure that is currently drawing attention (Weiss 1998). Current treatments require the injection of clot busting or anti-inflammatory drugs into the vein or surrounding region with micro-needles passed through the wall of the eye. Direct injection into the vein with surgeon-controlled micropipets is extremely difficult and requires great skill. Additionally, successful results from the treatment typically take several months to manifest. An externally controlled microrobotic platform could be used to locally deliver drugs with either micro-needles or drug releasing polymers and be left in the eye to perform follow up procedures as needed, without the need for multiple procedures.

Although electronic and mechanical systems have been miniaturized by VLSI and MEMS technologies, no counterpart to these exists for electro-chemical energy storage. Additionally, actuators that can be used for actuation or propulsion of integrated microsystems are also lacking (Dario et al. 1992). Currently, the only viable option for the actuation and steering of such a microrobot is external energy transfer. The use of magnetic fields generated ex-vivo for energy transfer and propulsion can provide a solution to this problem. Magnetic fields have a long history of being used to manipulate magnetic devices in the body (Gillies et al. 1994). Remote magnetic propulsion can be achieved with DC magnetic fields and gradients that produce translational forces on the device (Khamesee et al. 2002; Mathieu et al. 2003; Martel et al. 2004). Other methods of propulsion use rotating or oscillating magnetic fields to induce motions in the object to propel it through the environment (Sendoh et al. 1999; Ishiyama et al. 2000; Mei et al. 2002). In this paper a microfabricated prototype microrobot is introduced for use in a magnetic guidance and propulsion system. The nature of magnetic and viscous drag forces are discussed and experimental results on the mag-

The International Journal of Robotics Research
Vol. 25, No. 5–6, May–June 2006, pp. 527–536
DOI: 10.1177/0278364906065389
©2006 SAGE Publications
Figures appear in color online: <http://ijr.sagepub.com>

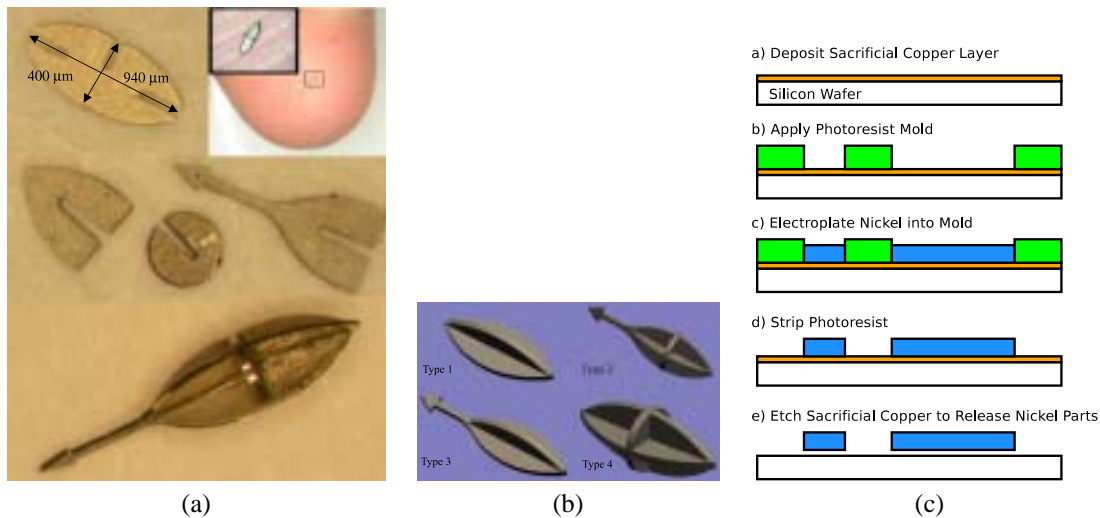


Fig. 1. a) Nickel microrobot components and an assembled microrobot. The inset shows another microrobot on a finger tip. b) Different configurations of microrobots. c) Manufacturing steps for the microrobots.

netic and drag properties of the microrobots are presented. With these results, the necessary magnetic field strengths for application inside different body-fluids are analyzed. Finally, a strategy for magnetic steering is proposed and a prototype steering system is presented.

2. Microrobot with Hybrid MEMS Design

The microrobot prototype is a three-dimensional structure built by microassembly of individual parts shown in Figure 1(a). Robot parts have been made with electroplated nickel, single crystal silicon, polymer and laser cut steel. The prototype robot used in the experiments reported in this paper was made from nickel which is not biocompatible, nor are other alloy materials with better magnetic properties which are being investigated for use. It is expected that the robot will be encapsulated with biocompatible steel or polymers such as parylene. Currently four different types of robots are being assembled from a combination of four basic parts and bonded with UV activated glue (Figure 1(b)). The winged-ellipsoid shape has an axis of symmetry along the long axis of the ellipsoid. An external magnetic field acts to align and pull the robot along this axis (i.e., magnetic torque and force) due to the shape anisotropy effect, much like a needle always becoming magnetized along its long axis. The winged shape also acts to reduce the side-ways drift of the microrobot by increasing the fluid drag along the axes perpendicular to the long axis.

The assembly process allows for the combination of incompatible materials and processes for the integration of MEMS based sensors and actuators. The significant advantage of the hybrid design is that the individual parts of the assembly can

be produced with standard MEMS manufacturing processes that create planar geometries. In this way, different subsystems of the robot can be manufactured using the most suitable process for the purpose. Figure 1(c) shows the steps of the micromanufacturing process for the nickel parts. Initially the wafers are cleaned and metallized with a titanium adhesion layer and sacrificial copper seed for subsequent electroplating. The thickness of the seed layer is 300 nm. After metallization the wafer is covered with a 80 μm thick layer of negative photoresist that is patterned to form the microrobot parts. The nickel parts are then deposited inside a bench top plating system at the rate of 1 μm/min to a thickness of 50 μm. Following the plating step, the photoresist is stripped and the copper seed layer is etched in a solution of ammonium persulfate which does not attack nickel.

3. Wireless Actuation through Ex-Vivo Magnetic Fields

3.1. Nature of Magnetic Forces

The primary vectors that define the magnetostatic field in magnetized matter are (external) magnetic field strength, \vec{H} (A/m), magnetization of the matter, \vec{M} (A/m), and magnetic flux density, \vec{B} (Tesla). The relationship between these vectors is

$$\vec{B} = \mu_0(\vec{H} + \vec{M}) \quad (1)$$

where μ_0 is the magnetic permeability of free space defined as $4\pi \times 10^{-7}$ Tm/A. For the idealized case of linear, isotropic, and homogeneous media the following relationships simplify (1) as

$$\vec{M} = \chi \vec{H} \quad (2)$$

$$\vec{B} = \mu_0(1 + \chi)\vec{H} = \mu_0\mu_r\vec{H} \quad (3)$$

where χ and μ_r are the susceptibility and relative permeability of the media, respectively. In general, these values are not constant but change with magnetization, approaching zero as the magnetization reaches a material dependent limit called the *saturation magnetization*, M_s . Within the saturation limits, the permeability can be thought of as an amplification factor that creates a net magnetic field inside the matter through an external field.

Ferromagnetic materials exhibit the largest relative permeability (on the order of 10^3 – 10^5). The dependence of magnetization on external fields (i.e., the M-H curve) for a ferromagnetic material is shown in Figure 2. The nonlinear response of the material also changes with its previous state of magnetization (indicating hysteresis). A ferromagnetic material magnetized to saturation will keep part of its magnetization (*remanent magnetization*, M_r) after the magnetizing field is taken away. It is necessary to apply a field H_{ci} (*intrinsic coercivity*) in the opposite direction of magnetization to cancel this magnetization. Soft magnetic materials (e.g., iron) are characterized by their high permeability and low coercivity ($H_{ci} < 10^3$ A/m) such that they can be easily magnetized and demagnetized by external fields. Hard magnetic materials (e.g., permanent magnets), have lower permeability but high coercivity ($H_{ci} > 10^4$ A/m) and large remnant magnetization. Once magnetized, they retain their magnetization against external fields. The magnetic force and torque that are exerted on an object with uniform magnetization \vec{M} in a magnetic field with flux density \vec{B} are defined as

$$\vec{F}_m = V_m(\vec{M} \cdot \nabla)\vec{B} \quad (4)$$

$$\vec{\tau}_m = V_m\vec{M} \times \vec{B} \quad (5)$$

where V_m is the volume of the magnetized object. Notice that the magnetic torque is dependent on the elements of \vec{B} whereas the magnetic force is dependent on the gradient of \vec{B} . In the case of hard magnetic materials with fixed \vec{M} , (5) can be applied directly. Soft magnetic materials require an energy balance analysis matching the shape anisotropy with the applied torque and magnetization. Geometries with large length to width ratios have very strong anisotropy and \vec{M} can be assumed to be within a few degrees of the easy axis (Judy 1994). Equations (4) and (5) indicate that magnetic forces are volumetric. Therefore, the required fields and field gradients to exert a certain torque and force on a magnetized object increase rapidly as the object becomes smaller.

3.2. Magnetic Properties of the Microrobot

The relationship between the external magnetic field and the resulting magnetization of the robot is dependent on geometry and material properties. However, the magnetic properties

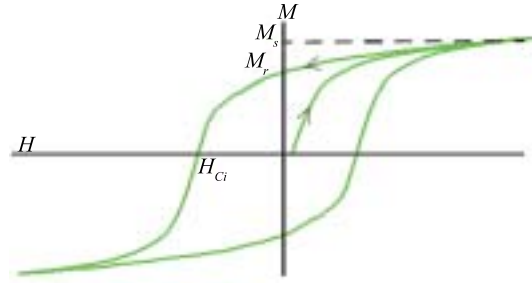


Fig. 2. Typical M-H curve of a ferromagnetic material.

of the material are also significantly affected by the manufacturing process, which is difficult to model. Therefore, it was necessary to perform experimental evaluation of the magnetization curve for the microrobots in order to obtain more reliable values. The microrobots were tested using a coercivity spectrometer. The results of this test covered the full range of magnetization as shown in Figure 3. The robots reached a saturation magnetization between 5 – 8×10^5 A/m at approximately 0.2 T external field.

Using permanent magnetic materials is an alternative to building the robot structure out of soft magnetic materials. The robot is then pre-magnetized, reducing the external field requirement during an operation and creating a constant direction of magnetization independent of shape anisotropy. A variety of techniques have been proposed for integrating hard magnetic materials into MEMS devices, including sputtering, thermal evaporation, assembly, electroplating, screen printing, spin coating, and molding. Each method offers its own advantages and disadvantages. Recent work (Vollmers et al. 2003) integrated NdFeB magnetic powder into MEMS devices with wafer-level processing. It resulted in magnets that are significantly thicker than thin film magnets, and utilized the superior magnetic properties of modern NdFeB material.

3.3. Fluid Drag Forces on the Microrobot

In addition to the magnetic forces analyzed above, gravitation/bouyancy and viscous fluid drag forces are also acting on the microrobot. The drag force can be expressed as

$$F_d = \frac{1}{2}C_d\rho_fAv^2 \quad (6)$$

where ρ is the density of the body fluid, A is the cross sectional area of the robot, v is the relative velocity of the robot with respect to the fluid media and C_d is the drag coefficient representing the overall effect of the robot's geometry on the drag force. However, the drag coefficient itself changes with the Reynolds Number, Re . For a spherical object in laminar flow regime (i.e., $Re < 1.0$) the drag coefficient can be approximated as

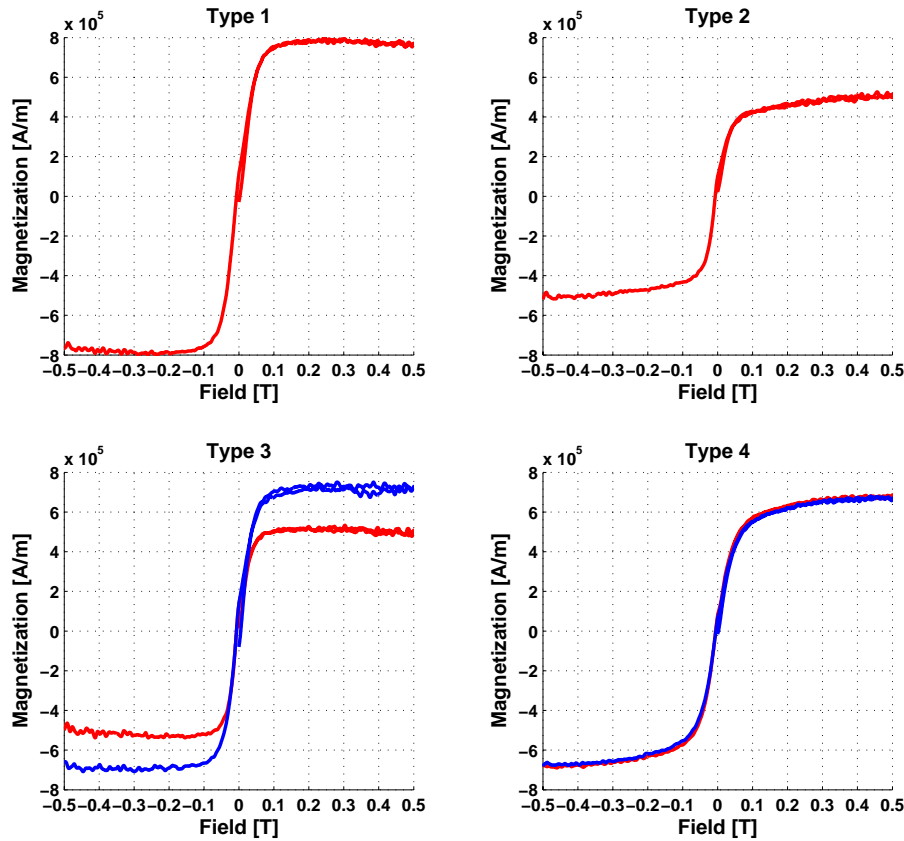


Fig. 3. Magnetization curves for the different types of microrobots (Figure 1(b)). Types 3 and 4 were tested with two different samples.

$$C_d = \frac{24}{Re} \quad (7)$$

$$Re = \frac{\rho_f D v}{\mu_f} \quad (8)$$

where D is the diameter of the sphere and μ_f is the dynamic viscosity of the fluid. Using (7) and substituting $A = \frac{1}{4}\pi D^2$, (6) can be simplified as

$$F_d = 3\pi\mu_f D v \quad (9)$$

In addition to the drag force, a net buoyancy force will be acting on the robot

$$F_b = V_r(\rho_r - \rho_f)g \quad (10)$$

where V_r and ρ_r are the density and volume of the robot, respectively, and g is the gravitational acceleration. The most important outcome of (4), (5), (6), and (10) is that, the fluid

drag forces are dependent on the area, whereas magnetic and buoyancy forces are volumetric. For this reason, as the size of the robot becomes smaller, the required field gradient to move at a particular speed rapidly increases.

Equation (9), also known as Stokes Drag, is frequently used for calculating the drag force on magnetic beads and other small particles, approximating their shape as a sphere (Holligan et al. 2003). Notice that the special case of (9) has linear dependency of the drag force on velocity whereas the general case of (6) indicates a quadratic relationship. We performed experiments in order to quantify the drag forces on the winged-ellipsoid shape of the microrobots.

3.4. Viscous Drag Force Experiments

The viscous drag force experiments were conducted by releasing the microrobots inside a chamber filled with a fluid of known viscosity and observing their velocity under the net

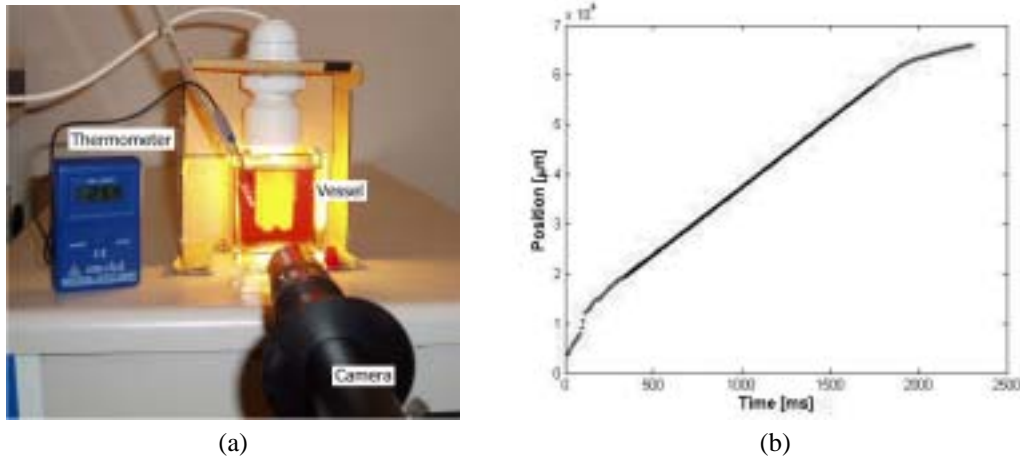


Fig. 4. a) Visual tracking setup for fluid drag experiments. b) Sample data from the fluid drag experiments. The perturbations at the ends of the line from the robot insertion and wall effects are excluded from the calculation.

effect of fluid drag, gravity, and buoyancy forces. Figure 4(a) shows the experimental setup. The motion of the microrobots were tracked using a microscope-camera system. Upon release from the top of the chamber the microrobots accelerate until the increasing drag force equals the net buoyancy force. Figure 4(b) shows the data collected from one of the experiments.

The experiments were performed using three different silicon oils, AK100, AK350, and AK1000, each having room temperature dynamic viscosities of 100, 350, and 1000 cP (centipoise) respectively. The actual viscosity values were corrected for the measured temperature of the chamber. The experimental setup was verified using steel ball-bearing spheres of known size and weight. The measurements for the steel spheres were within 5% of the calculated values.

The results of experiments indicated a linear dependency of the drag force on velocity, similar to the case of a sphere. A drag number, D_N was calculated as

$$D_N = \frac{F_d}{\mu_f v} \quad (11)$$

for each of the four types of the robot. The resulting data are shown in Figure 5. The box plots present the distribution of the repeated measurements. The height of the box indicates the interquartile range between the 25% and 75% percentiles of the data, while the line inside the box shows the median. The bars show the total spread of the measurement and the circles represent outlying data. The drag number measurements show a variation of about 15%, clustered around a value of 4.5×10^{-3} m. If this value is converted to an effective sphere

diameter through the relation $D_N = 3\pi D$ we find a diameter of $477 \mu\text{m}$ which is close to the cross-section diameter ($400 \mu\text{m}$) of the ellipsoid shape.

3.5. Required Magnetic Fields in Body Fluids

With the analysis of magnetic and viscous drag properties of the microrobots, the necessary magnetic field strengths for medical applications can be estimated. For this analysis the microrobots are assumed to be magnetized to saturation at 5×10^5 A/m. The volume of a Type 3 robot is ($3.22 \times 10^{-11} \text{m}^3$). For fluid drag, the average drag number of 4.5×10^{-3} m is used as an approximation.

The human eye, mostly filled by a transparent gel-like fluid called the vitreous humor, is one of the more promising proposed workspaces for a biomedical microrobot. The vitreous humor fills the posterior cavity of the eye between the lens and the retina (Chirilla and Young 1998). Although it is composed almost entirely of water (99%) it also contains a collagen fiber network, hyaluronic acid, and soluble proteins, and, therefore, has the properties of a viscoelastic liquid with high viscosity. Viscoelastic materials can be modeled by spring and dashpot elements representing the elastic and viscous characteristics of the material with shear modulus G and dynamic viscosity η . Two common models of viscoelastic behavior are the Maxwell and Kelvin elements that consist of a spring and a dashpot in series and in parallel, respectively (Figure 6).

A research study utilizing a specially built magnetic-bead rheometer device that performed non-destructive testing inside the eye has been reported by Lee (Lee 1992; Lee et al.

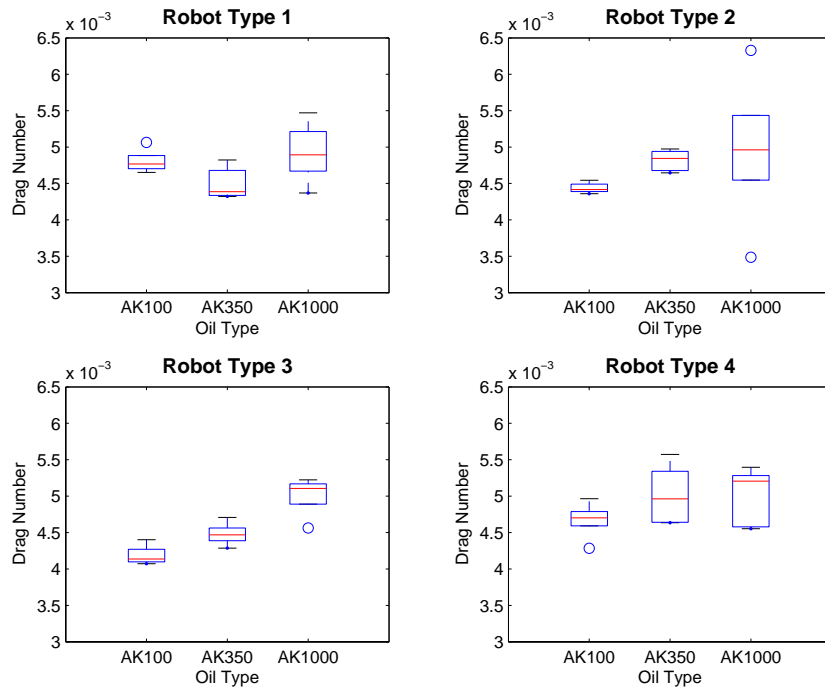
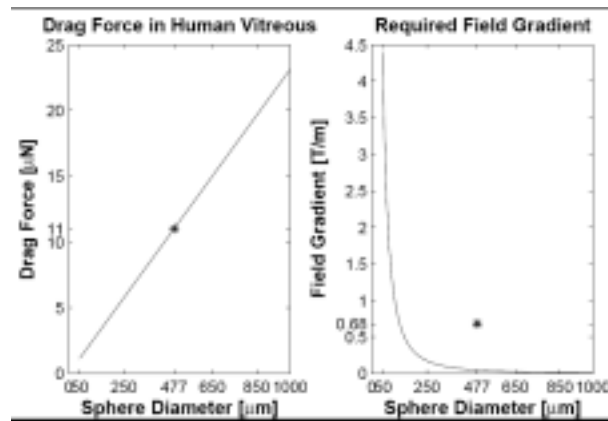
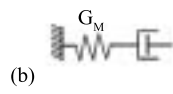


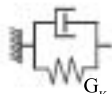
Fig. 5. Drag numbers calculated for each robot type for oils of three different viscosities.



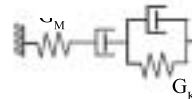
(a)



(b)



(b)



(c)

(c)

Fig. 6. a) Drag forces on a spherical magnet moving at 0.5 mm/s in the human vitreous and the required field gradient for various sphere diameters. Magnetization is $\vec{M} = 5 \times 10^5$ A/m and viscosity is 4900 cP. The value for the prototype microrobot is shown with *. b) Maxwell and Kelvin elements for describing the rheological properties of materials. c) Burgers model used by Lee, Litt, and Buchsbaum (1992) to model the vitreous humor.

1992). Lee uses the Burgers model that consists of a Maxwell and a Kelvin element in series to describe the properties of the vitreous (Figure 6(c)). Of the four parameters in this model, the viscosity of the Maxwell dashpot (η_M) represents the irreversible flow of the material under constant stress that is the main source of the viscous drag forces on the robot as it is steered inside the eye. The mean values of viscosity were 1398 cP at the anterior, 2179 cP at the central, and 4862 cP at the posterior regions. The values for the Kelvin viscosity were 4 to 10 times lower, further indicating the dominance of Maxwell viscosity for the drag force. Figure 6(a) shows the drag forces on a spherical shaped robot with a diameter between 50 to 1000 μm and magnetization $5 \times 10^5 \text{ A/m}$ moving inside the vitreous at a speed of 0.5 mm/s. The viscosity at the posterior region is used. In addition, the necessary field gradient to balance the drag forces are also shown. The location of the prototype microrobot with the winged-ellipsoid shape is also indicated.

For cardiovascular applications, the fluid media that the microrobot moves in is blood. The flow velocity of blood in the human body ranges between 0.05 m/s in the capillaries to 0.7 m/s at the exit of the aorta with a viscosity of about 2.8 cP (Despopoulos and Silbernagl 1991). Figure 7 shows the drag forces on the microrobot and the required field gradient to balance the robot against the flow. In addition to simple force generation, cardiovascular use of an untethered microrobot faces additional hurdles. Current imaging technology, specifically the MRI, can not yet provide high frame rate feedback with enough resolution to reliably control the robot (Martel et al. 2004). The frame rate requirements become even tougher when considering that blood flow becomes turbulent in select areas of the body, including the heart and in areas of heavy plaque deposits and rough artery walls.

4. Magnetic Steering System

Equations (4) and (5) suggest that controlled external magnetic fields can be used to induce torques and forces on a magnetized object and control its orientation and position. At the micro scale, active control and steering of magnetic beads in two and three dimensions have been demonstrated for DNA micromanipulation (Haber and Wirtz 2000) and for performing intracellular rheology and force measurements (Amblard et al. 2000; Vicci 2001). Whereas ferromagnetic materials exhibit higher susceptibility and saturation magnetization, the control of the beads' magnetization vector by external fields is difficult due to the hysteresis effect. Also, undesired interactions between magnetized beads can occur even after the external field has vanished. Superparamagnetic beads, which do not show hysteresis, are often used instead. The susceptibility of these beads, however, is much lower than ferromagnetic materials (e.g., 10^{-2} for commonly used M280 beads from Dynal Inc.; Amblard et al. 2000). Solenoid electromagnets

with soft magnetic poles are typically used to generate high field gradients, as much as 100 T/m across a 20 mm air gap (Haber and Wirtz 2000).

An important issue related to the control of a magnetic microrobot is the nonlinear nature of the field and gradients that are created by electromagnet coils. The field from an air-core solenoid coil along its axis is roughly proportional to the inverse square of the distance d to the solenoid. In this case the torque and force on the soft magnetic material are proportional to the fourth and fifth inverse power of the distance respectively, as shown in Figure 8.

One way of reducing the effect of such nonlinearities is to create uniform magnetic fields and field gradients using various coil configurations (Jin 1999). For example, the Helmholtz coil configuration consists of two identical coils that are placed on the same axis and separated by a distance equal to the radius of the coils. This arrangement generates a uniform field close to the center of the coil pair when current passes in the same direction in both coils. Similarly, the Maxwell coil configuration can generate a uniform gradient near the center when the coils are separated by $\sqrt{3}$ times the radius and the current passes in the opposite direction. Figure 9 shows the plot of the fields of Helmholtz and Maxwell coils. Both of these coils are commonly used in MRI systems. Although the uniform fields of commercial MRI machines are quite high (0.5–2.0 T), the gradient fields they can generate continuously are in the 0.01 to 0.05 T/m range and are limited by the capacity of the non-superconducting gradient coils needed for the rapidly changing field. While it is expected that the saturation magnetization of the material in the microrobot can be increased by a factor of 3 through the use of high saturation alloys, methods of generating higher field gradients will have to be developed before such a steering system can be used. Focusing on the generation of high field gradients over smaller volumes for ocular procedures is one option. Increasing the volume of the assembled robot is another possibility for some procedures.

The magnetic steering principle was investigated using a coil system as illustrated in Figure 10(a). The magnetic torque and force on the microrobot were controlled independently through the Maxwell and Helmholtz fields, respectively. This way the orientation and direction of motion of the microrobot could be commanded on a two dimensional plane. Steering tests were performed in a maze-like structure cut into a plastic substrate (Figure 10(b)). The water-filled channels were 1000 μm wide and 300 μm deep. The maze was fixed at the center of the rotating coils with a microscope camera system used to obtain a top view for vision feed back (Figure 10(c)). The orientation of the coils and propulsion of the robot was controlled through a PC interface. The experiments confirmed that the independent orientation/thrust control principle was successful. The video in Extension 1 shows the microrobot being steered inside the maze. The microrobot followed the orientation of the coils without translation unless the Maxwell

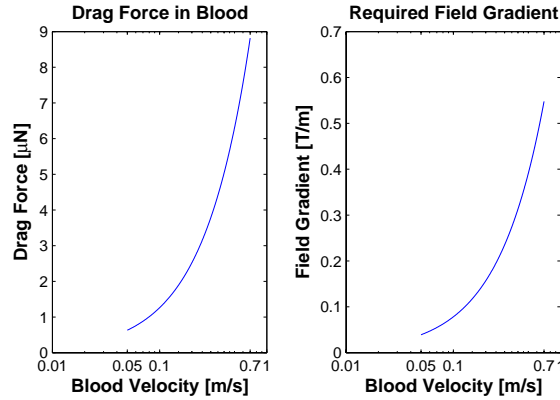


Fig. 7. Drag forces on the microrobot in human blood and the required field gradient to resist the fluid drag.

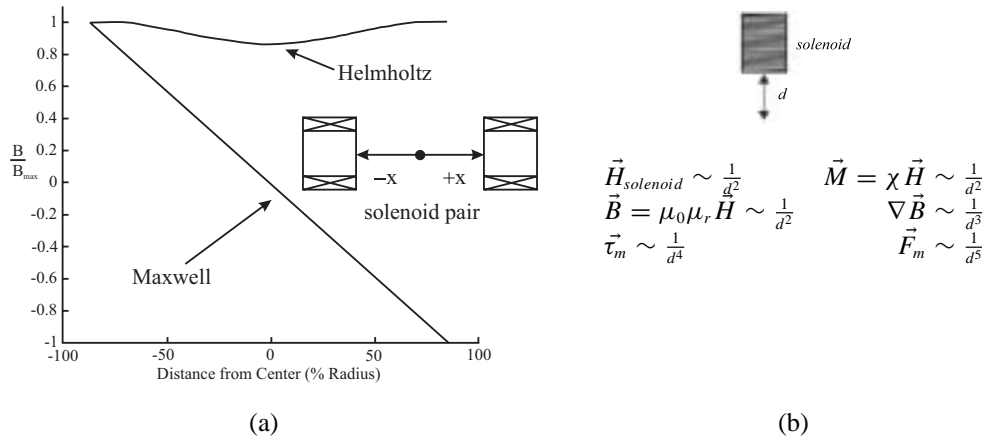


Fig. 8. a) Normalized magnetic field magnitudes along the central axes of Helmholtz and Maxwell coils. b) The force and torque on a soft magnetic object created by a solenoid coil.

coils are energized. Reversing the current in the Maxwell coils reversed the gradient and the robot moved backwards.

5. Conclusions

This paper investigated the idea of steering sub-mm sized untethered microrobots inside body fluids with external magnetic fields. A prototype microrobot and steering system were designed and built. Magnetization tests on the microrobots indicated that the robots reached saturation magnetization between $5\text{--}8 \times 10^5$ A/m at approximately 0.2 T external field. The fluid drag experiments showed a linear dependency of viscous drag forces on velocity. Estimations on the necessary field gradient to resist fluid drag forces in different body fluids showed that a minimum gradient of about 0.7 T/m would be necessary. A magnetic steering principle based on independent control of orientation and thrust with constant field and field-gradient generating coils was successfully tested. These results confirm that magnetic actuation is a suitable mode of

energy transfer for untethered biomedical microrobots. However, the disproportional scaling of magnetic and viscous drag forces dictates the need for higher magnetic-field gradients over larger areas than is currently available from similar magnetic systems such as MRI machines. This, combined with the need for high-frame-rate feedback, make ocular applications an ideal starting point for the development of biomicrobots.

Appendix: Index to Multimedia Extensions

The multimedia extension page is found at <http://www.ijr.org/>.

Table of Multimedia Extensions

Extension	Type	Description
1	Video	Magnetically driving the micro robot through the maze

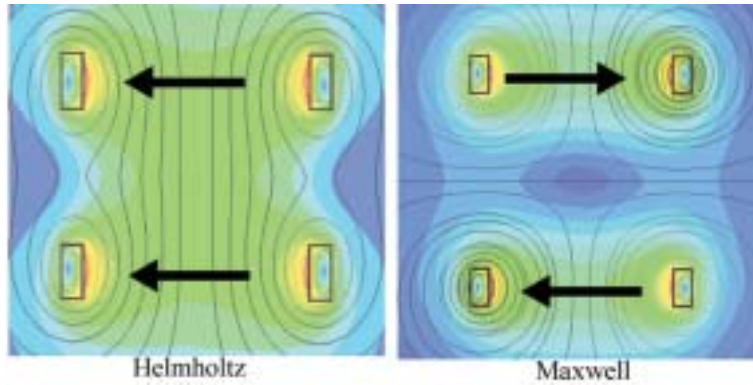


Fig. 9. Cross sectional view of the magnetic field and flux lines from Helmholtz and Maxwell coils. The Helmholtz coil produces a uniform field, while the Maxwell coil produces a field that goes to zero in the center (see Figure 8). Arrows indicate the direction of the current in each coil.

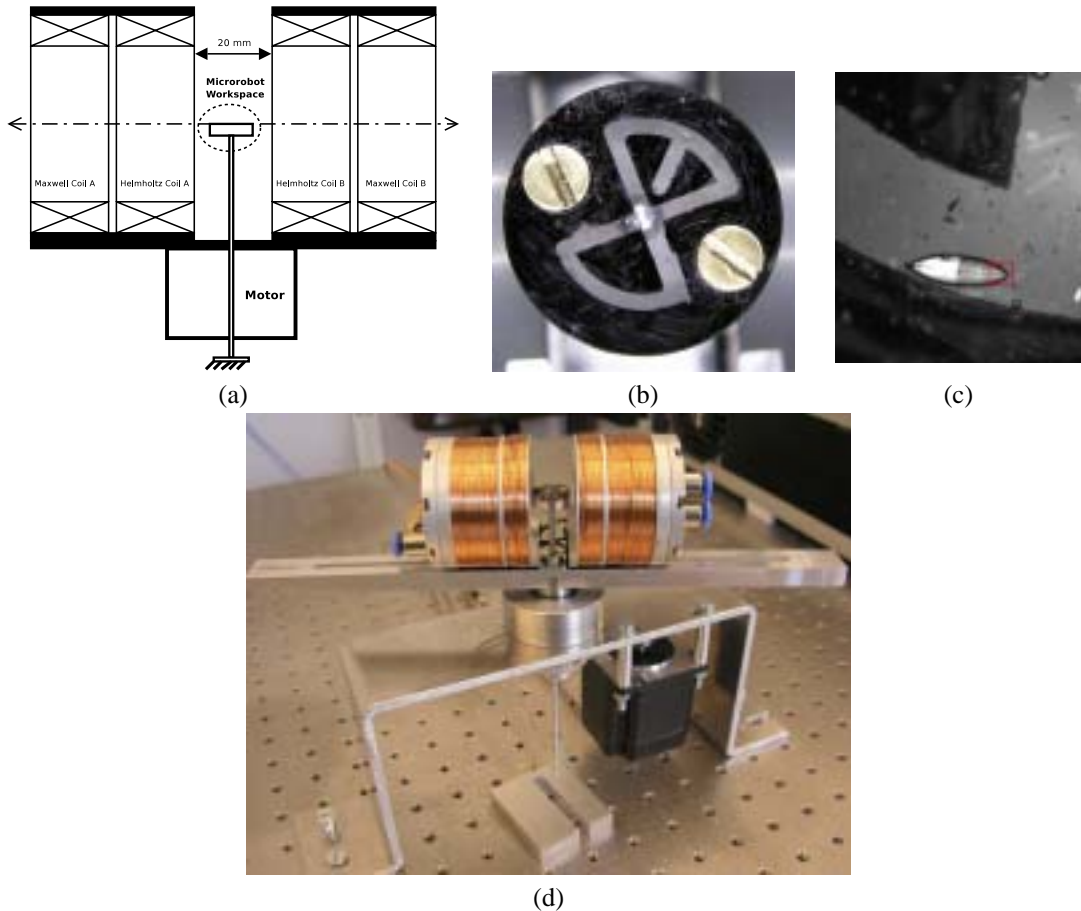


Fig. 10. a) Steering system with coaxial Maxwell and Helmholtz coil pairs. A maze structure is fixed at the center of the workspace between the coils. The coils can rotate about the workspace to control the orientation and direction of magnetic thrust vector. b) Microrobot steering maze. The channels are 1000 μm wide and 300 μm deep. The microrobot is also visible at the upper part. c) Magnified image of microrobot inside the maze. d) Magnetic steering system.

Acknowledgements

We would like to thank Dr. Friedrich Heller from the Institute of Geophysics, ETH Zürich, for his help with the magnetization measurements and Dr. med. Justus Garweg from Dept. of Ophthalmology, Inselspital Bern, for his guidance on vitreoretinal applications of the microrobot. This work is supported by Swiss National Science Foundation through the National Center of Competence in Research program for Computer Aided Image Guided Medical Interventions (NCCR Co-Me).

References

- Amblard, F., Yurke, B., Pargellis, A., and Leibler, S. 2000. A Magnetic Manipulator for Studying Local Rheology and Micromechanical Properties of Biological Systems. *Review of Scientific Instruments* 71(3):818–827.
- Chirilla, T. V. and Young, Y. 1998. The Vitreous Humor. In: *Handbook of Biomaterial Properties*, (eds. J. Black and G. Hastings), Chapman & Hall, London.
- Dario, P., Valleggi, R., Carrozza, M. C., Montesi, M. C., and Cocco, M. 1992. Microactuators for Microrobots: a critical survey. *Journal of Micromechanics and Microengineering* 2(3):141–157.
- Despououlos, A. and Silbernagl, S. 1991. *Color Atlas of Physiology*. New York: Thieme Medical Publishers, p. 156.
- Gillies, G. T., Ritter, R. C., Broadus, W. C., Grady, M. S., Howard, M. A. III, and McNeil, R. G. 1994. Magnetic Manipulation Instrumentation of Medical Physics Research. *Review of Scientific Instruments* 65(3):533–562.
- Haber, C. and Wirtz, D. 2000. Magnetic Tweezers for DNA Micromanipulation. *Review of Scientific Instruments* 71(12):4561–4570.
- Holligan, D. L., Gilles, G. T., and Dailey, J. P. 2003. Magnetic Guidance of Ferrofluidic Nanoparticles in an In Vitro Model of Intraocular Retinal Repair. *IOP Nanotechnology* 14:661–666.
- Ishiyama, K., Arai, K. I., Sendoh, M., and Yamazaki, A. 2000. Spiral-type Micromachine for Medical Applications. *Proc. 2000 International Symposium on Micromechanics and Human Science*, pp. 65–69.
- Jin, J. 1999. *Electromagnetic Analysis and Design in Magnetic Resonance Imaging*, Florida: CRC Press.
- Judy, J. W. 1994. *Magnetic Microactuators with Polysilicon Flexures*. M.S. Thesis. EECS Department, University of California, Berkeley.
- Khamesee, M. B., Kato, N., Nomura, Y., and Nakamura, T. 2002. Design and Control of a Microrobotic System Using Magnetic Levitation. *Transactions on Mechatronics* 7(1):1–14.
- Lee, B. 1992. *Comparative Rheological Studies of the Vitreous Body of the Eye*. PhD Thesis, University of Pennsylvania.
- Lee, B., Litt, M., and Buchsbaum, G. 1992. Rheology of the Vitreous Body. Part I: Viscoelasticity of Human Vitreous. *Biorheology* 29:521–533.
- Martel, S., Mathieu, J.-B., Felfoul, O., Macicior, H., Beaudoin, G., Soulez, G., and Yahia, L'H. 2004. Adapting MRI Systems to Propel and Guide Microdevices in the Human Blood Circulatory System. *Proceedings of the 26th annual International Conference of the IEEE EMBS*, pp. 1044–1047.
- Mathieu, J., Martel, S., Yahia, L., Soulez, G. and Beaudoin, G. 2003. Preliminary Studies for Using Magnetic Resonance Imaging Systems as a Mean of Propulsion for Microrobots in Blood Vessels and Evaluation of Ferromagnetic Artefacts. *IEEE CCECE Conf. on Elec. and Comp. Eng.*, pp. 835–838.
- Mei, T., Chen, Y., Fu, G., and Kong, D. 2002. Wireless Drive and Control of a Swimming Microrobot. *Proceedings of the 2002 IEEE International Conference on Robotics and Automation*, pp. 1131–1136.
- Sendoh, M., Ajiro, N., Ishiyama, K., Inoue, M., and Arai, K. I. 1999. Effect of Machine Shape on Swimming Properties of the Spiral-Type Magnetic Micro-Machine. *IEEE Transactions on Magnetics* 35(5):3688–3690.
- Vicci, L. 2001. *A 3D Magnetic Force Manipulator DC Prototype*, UNC Chapel Hill Dept. of Computer Science Technical Report, no. TR01-031.
- Vollmers, K., Anderson, R., Nelson, B. J., and Pepin, J. 2003. High Strength Rare Earth-Iron-Boron Printed Magnets Used in a Long Throw-High Force Electromagnetic Actuator With Microfabricated Coil. *IEEE Int. Conf. on MEMS (MEMS2003)*, pp. 60–63.
- Weiss, J. N. 1998. Treatment of Central Retinal Vein Occlusion by Injection of Tissue Plasminogen Activator Into a Retinal Vein. *American Journal of Ophthalmology* 126(1):142–144.